Analysis of Middle Frequency Resonance in DFIG System Considering Phase-Locked Loop

Yipeng Song, *Member, IEEE*, and Frede Blaabjerg, *Fellow, IEEE*

***Abstract*—As the wind power technology develops, the doubly fed induction generator (DFIG) based wind power system, when connected to a weak network with large impedance, may suffer resonances, i.e., subsynchronous resonance or high-frequency resonance when connected to the series- or parallel- weak network. Besides these two resonances, a middle frequency resonance (MFR) between 200 and 800 Hz may appear when the phase-locked loop (PLL) with fast control dynamics is applied. In order to analyze the MFR, the DFIG system impedance considering the PLL is studied based on the vector-oriented control strategy in rotor-side converter and grid-side converter. On the basis of the established impedance modeling of the DFIG system, it is found that the PLL with fast control dynamics may result in the occurrence of MFR due to a decreasing phase margin. The simulation results of both a 7.5 kW small-scale DFIG system and a 2 MW large-scale DFIG system are provided to validate the theoretical analysis of the MFR.**

***Index Terms*—Controller parameters, doubly fed induction generator (DFIG) system, middle frequency resonance (MFR), phase-locked loop (PLL), parallel-compensated weak network.**

I. Introduction

As THE wind power generation technologies are under rapid growth, an increasing amount of doubly fed induction generator (DFIG) based wind power system connected to a weak network may be seen, which includes the microgrid, off-shore grid, and other power systems with large impedance [1]–[7]. As a consequence of the impedance interaction between the DFIG system and the weak network with large impedance, several types of resonances need serious attention.

When connected to a series-compensated weak network, the subsynchronous resonance (SSR) below the fundamental frequency may happen [8]–[14]. In order to improve the transmission capability of the long-distance cables, the series capacitance is employed to reduce the electric length of the long-distance transmission line, which finally has the configuration of series-compensated weak network [8]–[14]. However, the SSR can unfortunately appear, and it is pointed out that the impedance interaction between the DFIG system and the series-compensated grid network is the direct cause of the SSR [8]–[14]. In order to conduct the theoretical analysis of the SSR, the DFIG system impedance modeling needs to be established as an analysis platform. In [8]–[10], Vieto and Sun developed the positive and negative impedance modeling using harmonic linearization method for the DFIG system. The influences of the rotor current control, phase-locked loop (PLL), and the various rotor speeds are also investigated. The impedance modeling of the entire DFIG system and the series-compensated weak grid network are also reported in [11] with the conclusion that the interaction between the electric network and the converter controller is the main contribution of the SSR behavior.

On the other hand, when connected to a parallel-compensated weak network, the high-frequency resonance (HFR) is likely to happen [15]–[17]. As it is discussed in [16], the HFR can be a consequence of the impedance interaction between the DFIG system and the parallel-compensated weak network. The frequency of HFR can be estimated based on the Bode diagram of the DFIG system impedance and the parallel-compensated weak network impedance as discussed in [16]. The influence of the current closed-loop control parameters and the rotor speed on the HFR are also investigated. Moreover, an active damping strategy for the HFR is proposed in [15] and [17] by inserting a virtual impedance into the DFIG system.

So far, the most popular control strategy in the DFIG systems is the vector-oriented control (VOC) which includes two different methods, i.e., stator-voltage-oriented control and stator-flux-oriented control. The stator-voltage-oriented control, which is discussed in this paper, requires an accurate phase angle information of the network voltage using a PLL unit [4]–[7] so the *d*-axis and *q*-axis components of the rotor current, stator current, and grid voltage can be precisely calculated by using the Park transformation and inverse Park transformation. It is obvious that the PLL plays a critical role in the VOC control by giving the network voltage phase angle, and consequently determines the accuracy of the rotor current closed-loop control in the rotor-side converter (RSC) and the grid current closed-loop control in the grid-side converter (GSC) [4]–[7]. Based on the above explanations, it is necessary to study the PLL when building up the DFIG system impedance modeling.

In the DFIG system SSR analysis, the PLL is investigated in [9] and [10]. It is pointed out that the larger proportional and integral parameters K_{ppll} and K_{ipll} of the PLL closed-loop control result in faster PLL control dynamics, and make the SSR more likely to happen due to a smaller phase margin.

Nevertheless, during the analysis of the HFR [15]–[17], the impedance modeling of the DFIG system does not take into consideration of the PLL effect. Neglecting the PLL is relatively

Manuscript received August 3, 2016; revised November 1, 2016 and December 24, 2016; accepted February 19, 2017. Date of publication February 22, 2017; date of current version October 6, 2017. Recommended for publication by Associate Editor Y. Sozer.

The authors are with the Department of Energy Technology, Aalborg University, Aalborg 9220 Denmark (e-mail: yis@et.aau.dk; fbl@et.aau.dk).

Color versions of one or more of the figures in this paper are available online at http://ieeexplore.ieee.org.

Digital Object Identifier 10.1109/TPEL.2017.2672867

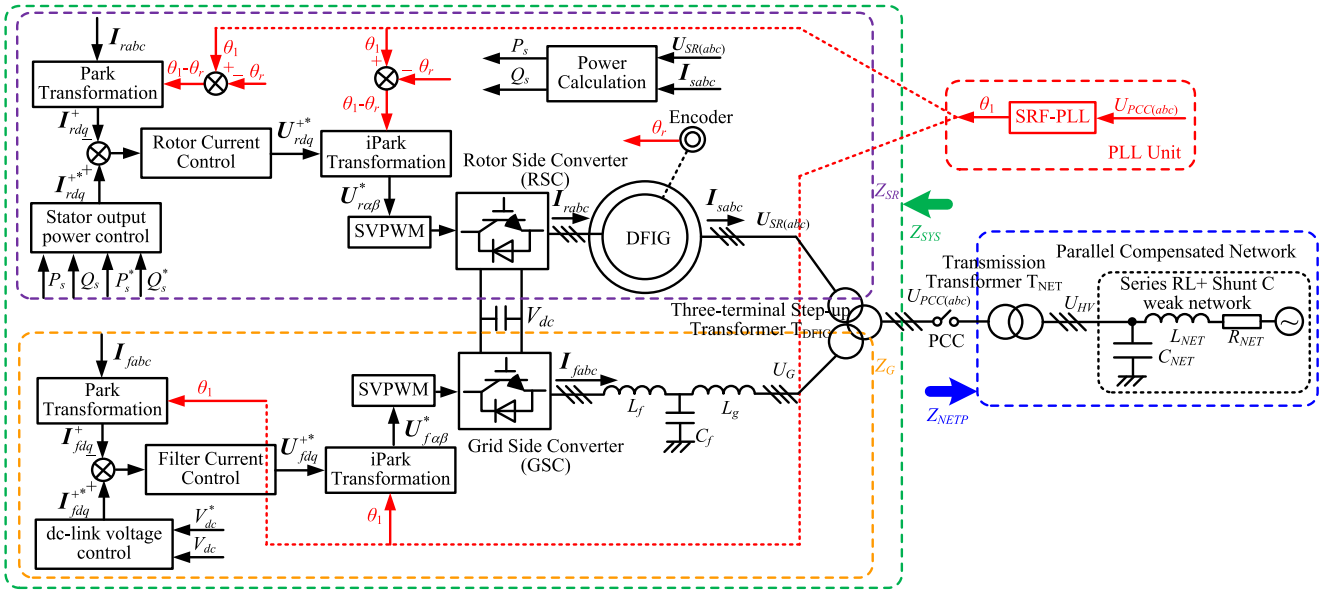

Fig. 1. Diagram of the DFIG system and the parallel-compensated weak network considering PLL. iPark means inverse park transformation.

reasonable since the investigated HFR is always above 1 kHz [15]–[17], while the typical control bandwidth of the PLL is lower than 100 Hz and as a result, the variations of the PLL proportional and integral parameters have negligible influence on the HFR performance.

The purpose of this paper is to investigate the influence of the PLL on the DFIG system impedance shape and to identify the potential resonances caused by PLL; and a DFIG system impedance modeling method is proposed on the basis of the VOC strategy for the RSC and the GSC with the inclusion of the PLL. Unlike the impedance modeling method in [8]–[10], which does not contain an explicit physical meaning, the proposed method is deduced based on the specific and detailed control units in the VOC, such as Park transformation, inverse Park transformation, current controller, and digital control delay. By including these units, the proposed method is more precise and helps us to better estimate the potential resonance caused by the PLL.

The impedance modeling of the PLL unit has been reported in the grid-connected voltage source converters connected to a weak network. The harmonic instability issue and the corresponding active damping strategies are studied in [18]–[29]. Several active damping strategies with virtual impedance are reported in [18]–[21] to mitigate the potential harmonic instability in the grid-connected converter, while the controller design is studied in details in [22] and [23] to improve the converter stability. The detrimental influence of the digital control delay on the converter stability is reduced in [24] and [25]. Furthermore, the impedance modeling of the grid-tied converter in the *dq* synchronous frame is proposed in [26] and [27]. Note that the impedance modeling of PLL unit in the DFIG system is mainly adopted from the work in [26], but it is modified in order better to analyze the influence of the PLL on the DFIG system stability.

It should be noted that, instead of the series-compensated weak network in [8]–[14], it is assumed in this paper that the DFIG system is connected to a parallel-compensated weak network. The parallel-compensated weak network is likely to exist in practice [15]–[17] since the power factor correction capacitances as well as the parasitic capacitances between the transmission cables and the ground are likely to occur and contribute to the parallel-connected capacitance.

It will be explained in this paper that the PLL using a fast control dynamics, i.e., large controller proportional and integral parameters K_{ppll} and K_{ipll}, will unfavorably reshape the DFIG system impedance having a larger phase response, and consequently produce a middle frequency resonance (MFR) between 200 and 800 Hz. Note that this type of resonance is between the frequency range of SSR and HFR, and all these three types of resonances in the DFIG system are caused by different reasons.

This paper is organized as follows: The impedance modeling of PLL unit is first established in Section II as a platform for the following analysis. Then, the impedance modeling of the DFIG machine and RSC, together with the impedance modeling of GSC and inductor-capacitor-inductor (LCL) filter, can be obtained with the PLL in Section III. The potential MFR is investigated with the different PLL proportional and integral parameters K_{ppll} and K_{ipll} values in Section IV. The simulation setup of the 2 MW large-scale DFIG system and the 7.5 kW small-scale DFIG system are built in order to validate the MFR in Section V. Finally, the conclusions are given in Section VI.

II. General Description and PLL Impedance Modeling

As the basic control foundation, the VOC strategy in the DFIG system requires an accurate reference frame transformation between the stationary frame and the synchronous frame for both rotor and grid currents and voltages. The grid voltage phase angle information is critical in this transformation, the PLL is able to pose its influence on the DFIG system through this critical phase angle information and it is essential to discuss the

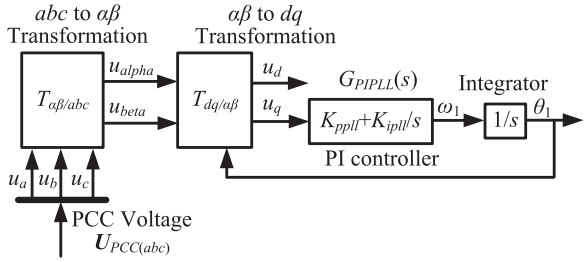

Fig. 2. Block diagram of the SRF-PLL used for DFIG synchronization.

reference frame transformation with the inclusion of the PLL unit during the DFIG system impedance modeling.

A. General Description of the Investigated DFIG System

Fig. 1 shows the diagram of the DFIG system and the parallel-compensated weak grid. The PLL is adopted to obtain the phase angle information of the voltage at the point of common coupling (PCC). Note that several kinds of PLLs can be applied, here the synchronous reference frame phase-locked loop (SRF-PLL) is chosen, which is explained in details in Fig. 2. The output of the PLL unit is the PCC voltage phase angle θ_1, which can be used in the control of the RSC and GSC.

The RSC contains the outer control loop of stator output active and reactive power P_s and Q_s, which gives out the rotor current reference value $\boldsymbol{I}_{\mathrm{rdq}}^{+*}$ in the synchronous frame. Then, the rotor current can be well controlled to deliver the expected wind power through the stator winding. It should be pointed out that during the control of rotor current, the Park transformation (*abc* to $\alpha\beta$ to *dq*) and inverse Park transformation (*dq* to $\alpha\beta$ to *abc*) is required for the reference frame transformation for the rotor current and the rotor control voltage, and the phase angle θ_1 of the voltage at PCC and the rotor position θ_r are necessary and critical information for this transformation. Note that in the following deduction, the outer control loop of stator output power is not included due to its relatively longer time constant.

On the other hand, the GSC has an outer control loop for the dc-link voltage control, which gives out the converter-side filter current reference value. Then, the filter current can be controlled in the synchronous frame. Similarly, this process also requires the information of the phase angle θ_1 of the voltage at the PCC to complete the reference frame transformation. Note that in the following deduction, the outer control loop for the dc-link voltage is not included due to its relatively longer time constant.

Based on above explanation, it can be seen that the PLL can pose its influence on the DFIG system performance by giving out the critical information of phase angle θ_1, then consequently influence the transformation results of the rotor/filter current and the control voltages, and further influence the current tracking accuracy.

A three-terminal step-up transformer T_{DFIG} is connected between the DFIG stator winding, the LCL output terminal, and the PCC for the purpose of increasing the voltage level of the DFIG system. In this paper, GSC output voltage $U_G = 480\,\mathrm{V}$, DFIG stator voltage $U_{SR} = 690$ V, PCC voltage $U_{\mathrm{PCC}} = 1$ kV and the parameters of this transformer can be found in Table II. The parallel-compensated weak network contains the network inductance L_{NET} and the network resistance R_{NET} in series connection, and the network shunt capacitance C_{NET} is connected between the transmission cables and the ground. A two-terminal transformer T_{NET} is connected between the PCC and the transmission cables, i.e., PCC voltage $U_{\mathrm{PCC}} = 1$ kV and high voltage $U_{\mathrm{HV}} = 25$ kV. The parameters of this transformer can be found in Table II.

B. Impedance Modeling of Reference Frame Transformation Considering PLL

The PLL unit is adopted to derive the PCC voltage phase angle information and in this paper the SRF-PLL is implemented [26]. The impedance modeling of SRF-PLL has been well developed in [26], but here for the sake of better illustration and discussion of the MFR, the impedance modeling of SRF-PLL still needs to be discussed.

Fig. 2 shows the block diagram of the SRF-PLL. As it is shown, the three-phase PCC voltage in the three-phase stationary frame u_{abc} is first under Clarke transformation, and the PCC voltage in the two-phase stationary frame $u_{\alpha\beta}$ can be obtained. Then, the Park transformation is adopted to transform the $u_{\alpha\beta}$ to the two-phase voltage in the synchronous frame u_{dq}. Thereafter, the *q*-component u_q is regulated to zero through the effective operation of the PI controller, and the output signal of the PI controller is the voltage angular speed ω_1, thus the voltage phase angle information θ_1 can be obtained with an integral unit. Note that this closed-loop control aims to regulate the voltage *q*-component u_q to zero, then the electric variables, including the stator voltage, rotor current, and stator current, can be aligned with the *d*-axis of the PCC voltage.

The transformation from u_{abc} to $u_{\alpha\beta}$ does not involve the voltage phase angle information and it is only a simple algebraic calculation as shown in the following equations. Thus, this Clarke transformation will not be included in the following impedance modeling of the PLL in order to keep it simple:

$$\begin{bmatrix} u_\alpha \\ u_\beta \end{bmatrix} = \begin{bmatrix} \frac{2}{3} & -\frac{1}{3} & -\frac{1}{3} \\ 0 & \frac{1}{\sqrt{3}} & -\frac{1}{\sqrt{3}} \end{bmatrix} \begin{bmatrix} u_a \\ u_b \\ u_c \end{bmatrix} \tag{1a}$$

$$T_{\alpha\beta/abc} = \begin{bmatrix} \frac{2}{3} & -\frac{1}{3} & -\frac{1}{3} \\ 0 & \frac{1}{\sqrt{3}} & -\frac{1}{\sqrt{3}} \end{bmatrix}. \tag{1b}$$

The transformation $T_{dq/\alpha\beta}$ from $u_{\alpha\beta}$ to u_{dq} can be presented as follows:

$$\begin{bmatrix} u_d \\ u_q \end{bmatrix} = \begin{bmatrix} \cos(\omega_1 \mathrm{t}) & \sin(\omega_1 \mathrm{t}) \\ -\sin(\omega_1 \mathrm{t}) & \cos(\omega_1 \mathrm{t}) \end{bmatrix} \begin{bmatrix} u_\alpha \\ u_\beta \end{bmatrix} \tag{2a}$$

$$T_{dq/\alpha\beta} = \begin{bmatrix} \cos(\omega_1 \mathrm{t}) & \sin(\omega_1 \mathrm{t}) \\ -\sin(\omega_1 \mathrm{t}) & \cos(\omega_1 \mathrm{t}) \end{bmatrix}. \tag{2b}$$

Based on (2), it can be seen that this transformation is nonlinear and its transfer function cannot be directly obtained. The small-signal modeling method [26] is adopted to deduce its transfer function. It is assumed that the PLL is in steady state, which means the phase angle difference between the actual phase angle of the grid voltage and estimated phase angle by the PLL is zero, and presented as follows:

$$\begin{bmatrix} u_d^{\mathrm{PLL}} \\ u_q^{\mathrm{PLL}} \end{bmatrix} = \begin{bmatrix} \cos(0) & \sin(0) \\ -\sin(0) & \cos(0) \end{bmatrix} \begin{bmatrix} u_d^{\mathrm{PCC}} \\ u_q^{\mathrm{PCC}} \end{bmatrix} \tag{3}$$

where superscript PLL indicates the components of the PLL control output and superscript PCC indicates the components of the PCC voltage. Note that since the phase angle difference between PLL output and PCC voltage is assumed to be zero, the right-hand side term in (3) is no longer $\alpha-$ and β-components in the two-phase stationary frame, but the *d*- and *q*-components in the synchronous frame.

A small perturbation is assumed to disturb this steady state, and the transfer function of the PLL unit can be derived by investigating the transient performance of the PLL to track precisely again the actual grid voltage phase angle [26].

Therefore, based on the small-signal perturbation method, (3) can be rewritten as

$$\begin{bmatrix} U_d^{\mathrm{PLL}} + \tilde{u}_d^{\mathrm{PLL}} \\ U_q^{\mathrm{PLL}} + \tilde{u}_q^{\mathrm{PLL}} \end{bmatrix} = \begin{bmatrix} \cos(0+\Delta\tilde{\theta}) & \sin(0+\Delta\tilde{\theta}) \\ -\sin(0+\Delta\tilde{\theta}) & \cos(0+\Delta\tilde{\theta}) \end{bmatrix} \begin{bmatrix} U_d^{\mathrm{PCC}} + \tilde{u}_d^{\mathrm{PCC}} \\ U_q^{\mathrm{PCC}} + \tilde{u}_q^{\mathrm{PCC}} \end{bmatrix} \tag{4}$$

where U_{dq}^{PLL} and U_{dq}^{PCC} are the *dq* steady signals of voltage via PLL output and voltage at PCC, respectively; while $\tilde{u}_{dq}^{\mathrm{PLL}}$ and $\tilde{u}_{dq}^{\mathrm{PCC}}$ are the *dq* small-signal perturbation of voltage via PLL output and voltage at PCC, respectively; and $\Delta\tilde{\theta}$ is the small-signal perturbation of the PLL output phase angle.

By using the small angle approximation of the trigonometric functions in (4), (5a) can be obtained. Furthermore, by removing the steady-state large signals from (5a), (5b) can be deduced as follows:

$$\begin{bmatrix} U_d^{\mathrm{PLL}} + \tilde{u}_d^{\mathrm{PLL}} \\ U_q^{\mathrm{PLL}} + \tilde{u}_q^{\mathrm{PLL}} \end{bmatrix} \approx \begin{bmatrix} 1 & \Delta\tilde{\theta} \\ -\Delta\tilde{\theta} & 1 \end{bmatrix} \begin{bmatrix} U_d^{\mathrm{PCC}} + \tilde{u}_d^{\mathrm{PCC}} \\ U_q^{\mathrm{PCC}} + \tilde{u}_q^{\mathrm{PCC}} \end{bmatrix} \tag{5a}$$

$$\begin{bmatrix} \tilde{u}_d^{\mathrm{PLL}} \\ \tilde{u}_q^{\mathrm{PLL}} \end{bmatrix} \approx \begin{bmatrix} \tilde{u}_d^{\mathrm{PCC}} + U_q^{\mathrm{PCC}}\Delta\tilde{\theta} \\ -U_d^{\mathrm{PCC}}\Delta\tilde{\theta} + \tilde{u}_q^{\mathrm{PCC}} \end{bmatrix}. \tag{5b}$$

According to Fig. 2, the small-signal perturbation of the PLL output phase angle can be presented as

$$\Delta\tilde{\theta} = \tilde{u}_q^{\mathrm{PLL}} G_{\mathrm{PIPLL}}(s)\frac{1}{s} \tag{6}$$

where $G_{\mathrm{PIPLL}}(s) = K_{\mathrm{ppll}} + K_{\mathrm{ipll}}/s$ is the PI controller in the PLL unit.

Thus, based on (5b) and (6), the relationship between the PLL output phase angle and the *q*-component of PCC voltage can be presented as [26] follows:

$$\Delta\tilde{\theta} = \frac{G_{\mathrm{PIPLL}}(s)}{s + U_d^{\mathrm{PCC}} G_{\mathrm{PIPLL}}(s)}\tilde{u}_q^{\mathrm{PCC}}. \tag{7}$$

Based on (7), the transfer function $T_{\mathrm{PLL}}(s)$ from the *q*-component of the PCC voltage to the PLL output phase angle can be presented as

$$\Delta\tilde{\theta} = T_{\mathrm{PLL}}(s)\tilde{u}_q^{\mathrm{PCC}} \tag{8a}$$

$$T_{\mathrm{PLL}}(s) = \frac{G_{\mathrm{PIPLL}}(s)}{s + U_d^{\mathrm{PCC}} G_{\mathrm{PIPLL}}(s)}. \tag{8b}$$

By substituting (8a) back into (5b), the following expression can be deduced:

$$\begin{aligned} \begin{bmatrix} \tilde{u}_d^{\mathrm{PLL}} \\ \tilde{u}_q^{\mathrm{PLL}} \end{bmatrix} &\approx \begin{bmatrix} \tilde{u}_d^{\mathrm{PCC}} + U_q^{\mathrm{PCC}} T_{\mathrm{PLL}}(s)\tilde{u}_q^{\mathrm{PCC}} \\ -U_d^{\mathrm{PCC}} T_{\mathrm{PLL}}(s)\tilde{u}_q^{\mathrm{PCC}} + \tilde{u}_q^{\mathrm{PCC}} \end{bmatrix} \\ &= \begin{bmatrix} 1 & U_q^{\mathrm{PCC}} T_{\mathrm{PLL}}(s) \\ 0 & 1 - U_d^{\mathrm{PCC}} T_{\mathrm{PLL}}(s) \end{bmatrix} \begin{bmatrix} \tilde{u}_d^{\mathrm{PCC}} \\ \tilde{u}_q^{\mathrm{PCC}} \end{bmatrix}. \end{aligned} \tag{9}$$

It needs to be noted that the mathematical deduction result in (9) considers the small-signal perturbation components, and this result remains true for the case of steady-state large signal in (2). As a result, (9) can be regarded as a closed-loop transfer function matrix from $\alpha\beta$ components to the *dq* components of the electric variables (including the three units, i.e., the transformation $T_{dq/\alpha\beta}$ from $u_{\alpha\beta}$ to u_{dq}, the PI controller for PLL, and the integral unit 1/s, as shown in Fig. 2), thus the transfer function matrix from $\alpha\beta$ components to the *dq* components can finally be derived as [26] follows:

$$G_{dq/\alpha\beta}(s) = \begin{bmatrix} 1 & 0 \\ 0 & 1 - U_d^{\mathrm{PCC}} T_{\mathrm{PLL}}(s) \end{bmatrix} \tag{10}$$

where the steady-state PCC voltage *q*-component U_q^{PCC} is zero, $T_{\mathrm{PLL}}(s)$ is defined in (8b).

It is important to point out that, although (10) is deduced based on the voltage components of the PLL and the PCC, it can also be used for the current component transformation. Moreover, it is seen that the information of the PLL is included in (10), thus the influence of PLL on the DFIG system impedance can be investigated based on (10).

Similarly, the closed-loop transfer function matrix from *dq* components to the $\alpha\beta$ components of the electric variables can be derived as given in the following.

Similar as (2a) and (2b), the transformation $T_{\alpha\beta/dq}$ from u_{dq} to $u_{\alpha\beta}$ can be presented as follows:

$$\begin{bmatrix} u_\alpha \\ u_\beta \end{bmatrix} = \begin{bmatrix} \cos(\omega_1 \mathrm{t}) & -\sin(\omega_1 \mathrm{t}) \\ \sin(\omega_1 \mathrm{t}) & \cos(\omega_1 \mathrm{t}) \end{bmatrix} \begin{bmatrix} u_d \\ u_q \end{bmatrix} \tag{11a}$$

$$T_{\alpha\beta/dq} = \begin{bmatrix} \cos(\omega_1 \mathrm{t}) & -\sin(\omega_1 \mathrm{t}) \\ \sin(\omega_1 \mathrm{t}) & \cos(\omega_1 \mathrm{t}) \end{bmatrix}. \tag{11b}$$

By adopting the small-signal perturbation method, the following equations can be obtained:

$$\begin{bmatrix} U_d^{\mathrm{PCC}} + \tilde{u}_d^{\mathrm{PCC}} \\ U_q^{\mathrm{PCC}} + \tilde{u}_q^{\mathrm{PCC}} \end{bmatrix} \approx \begin{bmatrix} 1 & -\Delta\tilde{\theta} \\ \Delta\tilde{\theta} & 1 \end{bmatrix} \begin{bmatrix} U_d^{\mathrm{PLL}} + \tilde{u}_d^{\mathrm{PLL}} \\ U_q^{\mathrm{PLL}} + \tilde{u}_q^{\mathrm{PLL}} \end{bmatrix} \quad (12a)$$

$$\begin{bmatrix} \tilde{u}_d^{\mathrm{PCC}} \\ \tilde{u}_q^{\mathrm{PCC}} \end{bmatrix} \approx \begin{bmatrix} \tilde{u}_d^{\mathrm{PLL}} - U_q^{\mathrm{PLL}}\Delta\tilde{\theta} \\ U_d^{\mathrm{PLL}}\Delta\tilde{\theta} + \tilde{u}_q^{\mathrm{PLL}} \end{bmatrix}. \quad (12b)$$

By substituting (8a) into (12b), the following expression can be deduced:

$$\begin{aligned} \begin{bmatrix} \tilde{u}_d^{\mathrm{PCC}} \\ \tilde{u}_q^{\mathrm{PCC}} \end{bmatrix} &\approx \begin{bmatrix} \tilde{u}_d^{\mathrm{PLL}} - U_q^{\mathrm{PLL}} T_{\mathrm{PLL}}(s)\tilde{u}_q^{\mathrm{PLL}} \\ U_d^{\mathrm{PLL}} T_{\mathrm{PLL}}(s)\tilde{u}_q^{\mathrm{PLL}} + \tilde{u}_q^{\mathrm{PLL}} \end{bmatrix} \\ &= \begin{bmatrix} 1 & -U_q^{\mathrm{PLL}} T_{\mathrm{PLL}}(s) \\ 0 & 1 + U_d^{\mathrm{PLL}} T_{\mathrm{PLL}}(s) \end{bmatrix} \begin{bmatrix} \tilde{u}_d^{\mathrm{PLL}} \\ \tilde{u}_q^{\mathrm{PLL}} \end{bmatrix}. \end{aligned} \quad (13)$$

It needs to be noted that the mathematical deduction result in (13) considers the small-signal perturbation components, and this result remains true for the case of steady-state large signal in (11). As a result, (13) can be regarded as the closed-loop transfer function matrix from *dq* components to the $\alpha\beta$ components of the electric variable (including the transformation $T_{\alpha\beta/dq}$ from u_{dq} to $u_{\alpha\beta}$, the PI controller for PLL and the integral unit 1/s, as shown in Fig. 2), and it can finally be derived as

$$G_{\alpha\beta/dq}(s) = \begin{bmatrix} 1 & 0 \\ 0 & 1 + U_d^{\mathrm{PLL}} T_{\mathrm{PLL}}(s) \end{bmatrix} \quad (14)$$

where the steady-state PLL voltage *q*-component U_q^{PLL} is zero, while the PLL voltage *d*-component U_d^{PLL} is equal to the PCC voltage *d*-component U_d^{PCC} in steady state. The $T_{\mathrm{PLL}}(s)$ is defined as given in (8b).

Similar to (10), (14) can be used to transform the current variables, and the information of the PLL is included, which means this transfer function matrix in (14) is able to demonstrate the influence of the PLL on the DFIG system impedance as well.

Based on (10) and (14), several conclusions can be drawn:

1) Both the $G_{dq/\alpha\beta}$ in (10) concerning $\alpha\beta$ to *dq* transformation, and the $G_{\alpha\beta/dq}$ in (14) concerning *dq* to $\alpha\beta$ transformation involve the PLL unit information. Thereafter, the influence of the PLL on the DFIG system impedance can be investigated by incorporating these two transformation units into the DFIG system impedance modeling process;
2) The *d*-axis and *q*-axis components are decoupled and the complexity of the DFIG system *dq*-axis coupling can be avoided, and the impedance modeling results can be easier to understand;
3) The PLL has influence on the β-axis of the DFIG system, but no influence on the α-axis. However, due to the decoupling compensation terms in the VOC, a resonance will still exist in both axes, as it will be explained in following.

III. DFIG System Impedance Modeling Considering PLL Unit

The above section has built up the impedance modeling of the reference frame transformation considering the PLL. Based on these results, the impedance modeling of the DFIG system can be established, and in this paper the PLL is introduced through the reference frame transformation deduced above.

A. Brief Introduction of the VOC Strategy

Before building up the DFIG system impedance, the control structure of the VOC strategy needs to be briefly illustrated, thereafter the impedance modeling of the DFIG system can better be discussed based on this description.

Fig. 3 shows the diagram of the rotor current controller for the RSC of the DFIG system: (a) total control diagram and (b) simplified control diagram.

As it is shown in Fig. 3(a), in the VOC strategy, the three-phase rotor current in the stationary frame $\boldsymbol{I}_{rabc}$ is first transformed to $\boldsymbol{I}_{r\alpha\beta}$ in the two-phase $\alpha\beta$ stationary frame, then based on the PCC voltage phase angle θ_1 obtained by the PLL and the rotor position θ_r by an encoder, the rotor current can be transformed to $\boldsymbol{I}_{rdq}$ in the two-phase *dq* synchronous frame. By comparing the actual rotor current value $\boldsymbol{I}_{rdq}^{+}$ and the reference value $\boldsymbol{I}_{rdq}^{+*}$, its error can be regulated by a PI controller $G_{\mathrm{PIRSC}}(s)$, and the inevitable digital control delay $G_d(s)$ always exists. The rotor control voltage $\boldsymbol{U}_{rdq}^{*}$ can be calculated as the sum of the PI controller output and the decoupling compensation terms [4]. Then, the rotor control voltage $\boldsymbol{U}_{rdq}^{+*}$ can be transformed to the $\boldsymbol{U}_{r\alpha\beta}^{*}$ using the information of θ_1 and θ_r, and further to the three-phase stationary components $\boldsymbol{U}_{rabc}^{*}$. The voltage posed on the DFIG machine can be calculated as $\boldsymbol{U}_{rabc}^{*} - \boldsymbol{U}_{SRabc}$ (defined in Fig. 1), and the rotor current can be obtained by the DFIG machine transfer function (will be illustrated in the following).

Obviously, the transformation from *abc* to $\alpha\beta$ and $\alpha\beta$ to *abc* is irrelevant to any phase angle, but only contains constant coefficient as shown in (1b). Thus, neglecting this transformation unit does not interfere with the PLL and the DFIG system, but helps to ease the complexity of the DFIG system impedance modeling. Moreover, the rotor position θ_r is given by an encoder, and it is assumed to be precise and irrelevant to the PLL and DFIG system control. Thus, the rotor position θ_r can also be removed from the control diagram.

Therefore, based on the above explanations, the transformations from *abc* to $\alpha\beta$ and $\alpha\beta$ to *abc*, as well as the rotor position θ_r, are removed, and a simplified control diagram is shown in Fig. 3(b).

B. Control Units and DFIG Machine Impedance Modeling

Based on Fig. 3(b), several control units and DFIG machine impedance modeling need to be discussed.

The rotor current PI controller can be presented as

$$G_{\mathrm{PIRSC}}(s) = K_{\mathrm{prsc}} + K_{\mathrm{irsc}}/s \quad (15)$$

where K_{prsc} and K_{irsc} are the proportional and integral parameters for rotor current control in RSC, respectively.

The inevitable digital control delay of 1.5 sampling periods [18]–[21] can be presented as

$$G_d(s) = e^{-sT_d} \quad (16)$$

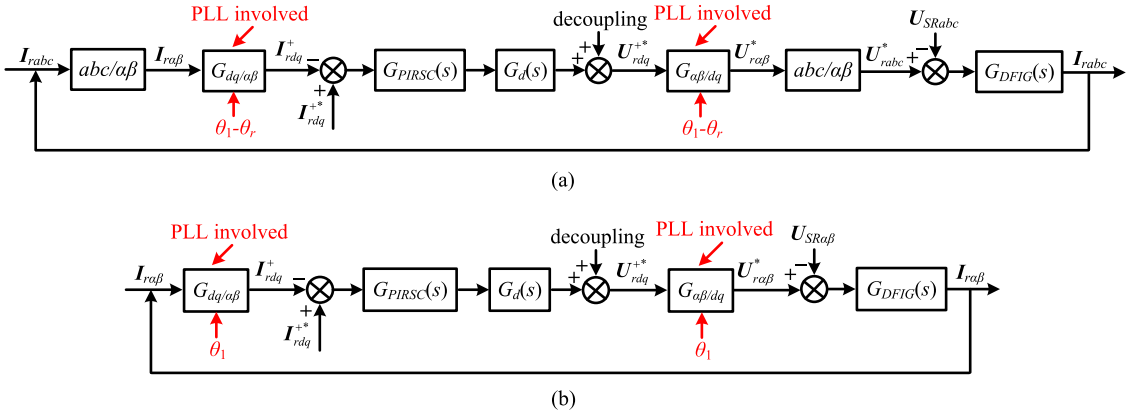

Fig. 3. Diagram of the rotor current in the RSC of the DFIG system: (a) total control diagram and (b) simplified control diagram neglecting the rotor position angle θ_r, the transformation from *abc* to $\alpha\beta$ and $\alpha\beta$ to *abc* reference frame.

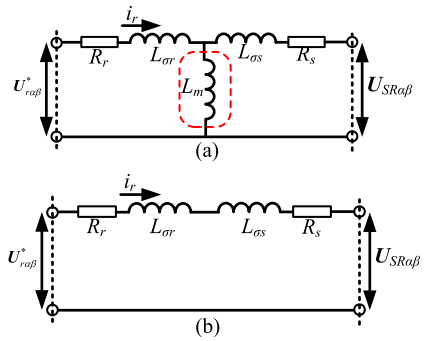

Fig. 4. Equivalent circuit of the DFIG machine: (a) total circuit and (b) simplified circuit.

where T_d is the digital control delay of 1.5 sampling periods.

The equivalent circuit of the DFIG machine [11] can be presented in Fig. 4. Since the mutual inductance L_m in both the small-scale and large-scale DFIG systems discussed in this paper is much larger than the stator and rotor leakage inductance $L_{\sigma s}$ and $L_{\sigma r}$, the mutual inductance branch can be neglected [11]. A simplified DFIG equivalent circuit can be seen in Fig. 4(b).

Obviously, according to Fig. 4(b), the DFIG machine impedance expression can be obtained as

$$G_{\mathrm{DFIG}}(s)=\frac{\mathrm{I}_{s\alpha\beta}}{\mathrm{U}^{*}_{r\alpha\beta}-\mathrm{U}_{\mathrm{SR}\alpha\beta}}=\frac{1}{R_r+sL_{\sigma r}+sL_{\sigma s}+R_s} \tag{17}$$

where R_r and R_s are the rotor and stator resistance, $L_{\sigma s}$ and $L_{\sigma r}$ are the stator and rotor leakage inductances. Note that, the stator branch and rotor branch in the simplified circuit are in series connection, thus the rotor current and stator current are the same.

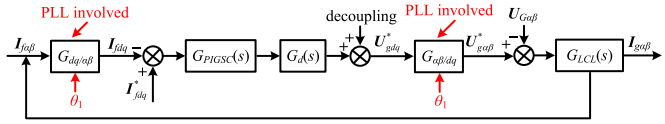

Fig. 5. Diagram of the grid current controller in the GSC of the DFIG system.

Thereafter, based on Fig. 3(b), the impedance of the DFIG rotor part seen from the PCC can be obtained as

$$\begin{aligned}Z_{\mathrm{SR}}(s)&=K_1^2\frac{\mathrm{U}_{\mathrm{SR}\alpha\beta}}{-\mathrm{I}_{s\alpha\beta}}\\&=K_1^2\frac{1+G_{\mathrm{DFIG}}(s)G_{dq/\alpha\beta}(s)G_{\mathrm{PIRSC}}(s)G_d(s)G_{\alpha\beta/dq}(s)}{G_{\mathrm{DFIG}}(s)}\end{aligned} \tag{18}$$

where $K_1=U_{\mathrm{PCC}}/U_{\mathrm{SR}}$ is the voltage ratio between PCC voltage U_{PCC} and stator winding voltage U_{SR}.

According to (10) and (14), the impedance of the DFIG rotor part in (18) actually contains both α-axis and β-axis components, thus it is better to separate these two components as (19a) and (19b) shown at the bottom of the page.

As it can be seen by comparing (19a) and (19b), the PLL-related reference frame transformation is involved only in the β-axis in (19b), but not in the α-axis in (19a).

C. GSC and LCL Filter Impedance Modeling

Similar as the case of RSC and DFIG machine impedance modeling, the GSC and LCL filter impedance modeling can be obtained based on the control diagram of the grid current controller, as shown in Fig. 5. Note that the C_f filter in the LCL filter has much larger reactance than the L_f and L_g components and thus it is assumed that $\boldsymbol{I}_{f\alpha\beta}$ and $\boldsymbol{I}_{g\alpha\beta}$ are almost equal.

$$Z_{\mathrm{SR}\alpha}(s)=K_1^2\frac{\mathrm{U}_{\mathrm{SR}\alpha}}{-\mathrm{I}_{s\alpha}}=K_1^2\frac{1+G_{\mathrm{DFIG}}(s)G_{\mathrm{PIRSC}}(s)G_d(s)}{G_{\mathrm{DFIG}}(s)} \tag{19a}$$

$$Z_{\mathrm{SR}\beta}(s)=K_1^2\frac{\mathrm{U}_{\mathrm{SR}\beta}}{-\mathrm{I}_{s\beta}}=K_1^2\frac{1+G_{\mathrm{DFIG}}(s)\left(1-U_d^{\mathrm{PCC}}T_{\mathrm{PLL}}(s)\right)G_{\mathrm{PIRSC}}(s)G_d(s)\left(1+U_d^{\mathrm{PLL}}T_{\mathrm{PLL}}(s)\right)}{G_{\mathrm{DFIG}}(s)}. \tag{19b}$$

Then, the LCL filter impedance modeling can be established as

$$G_{\mathrm{LCL}}(s)=\frac{\mathrm{I}_{g\alpha\beta}}{\mathrm{U}^{*}_{g\alpha\beta}-\mathrm{U}_{G\alpha\beta}}=\frac{1}{sL_g+\frac{sL_f*1/sC_f}{sL_f+1/sC_f}}. \quad (20)$$

Based on Fig. 5, the impedance of the DFIG grid part seen from the PCC can be obtained as

$$Z_G(s)=K_2^2\frac{\mathrm{U}_{G\alpha\beta}}{-\mathrm{I}_{g\alpha\beta}}$$

$$=K_2^2\frac{1+G_{\mathrm{LCL}}(s)G_{dq/\alpha\beta}(s)G_{\mathrm{PIGSC}}(s)G_d(s)G_{\alpha\beta/dq}(s)}{G_{\mathrm{LCL}}(s)} \quad (21)$$

where $K_2=U_{\mathrm{PCC}}/U_G$ is the voltage ratio between the PCC voltage U_{PCC} and the LCL output voltage U_G.

Similarly, (21) contains also both α-axis and β-axis components, respectively, and they can be separately written as (22a) and (22b) shown at the bottom of the page.

D. DFIG System Impedance Modeling

Once the impedances of the rotor part (including the RSC and DFIG machine) and the grid part (including the GSC and LCL filter) have been obtained in (19) and (22), the impedance modeling of the DFIG system Z_{SYS} can be calculated according to the parallel connection of these two parts, expressed in α-axis and β-axis components respectively as given in the following equations:

$$Z_{\mathrm{SYS}\alpha}(s)=\frac{Z_{\mathrm{SR}\alpha}(s)Z_{G\alpha}(s)}{Z_{\mathrm{SR}\alpha}(s)+Z_{G\alpha}(s)} \quad (23a)$$

$$Z_{\mathrm{SYS}\beta}(s)=\frac{Z_{\mathrm{SR}\beta}(s)Z_{G\beta}(s)}{Z_{\mathrm{SR}\beta}(s)+Z_{G\beta}(s)}. \quad (23b)$$

E. Parameter Variation and Magnetic Saturation

The parameter variations and saturation may be present in the DFIG system and it is not included in the simplified DFIG system impedance modeling. Following can be stated in respect to the parameter variations and saturation:

1) Based on the impedance modeling result of the DFIG system as shown in in Fig. 4, it can be found that the main parameters of the DFIG impedance modeling are the stator and rotor resistances and leakage inductances, and the mutual inductance.
2) Obviously, the parameter variation is likely to occur in the stator and rotor resistances and leakage inductances. Considering that the leakage inductances play a more important role than the resistances, it can be assumed that the parameter variation mainly happens in the stator and rotor leakage inductances.
3) In practice, the magnetic saturation in the DFIG system might happen, as a consequence the mutual inductance may vary.

Nevertheless, it should be pointed out that

1) Since the mutual inductance value is much larger than the stator and rotor leakage inductances in both small- and large-scale DFIG system as given in Tables I and II, the mutual inductance can be neglected even though it has a variation due to its larger value.
2) For the parameter variations in the stator and rotor leakage inductance, since their value are very small in both the small- and large-scale DFIG system, the variation is also very small, thus little influence on the DFIG system impedance will be seen.

In conclusion, based on the above explanations, it can be found that, even the parameters variation and magnetic saturation may occur in practice, their influence on the DFIG system impedance can be neglected, thus it will not be discussed in detail in this paper due to the limited space.

TABLE I
PARAMETERS OF 7.5 KW SMALL-SCALE DFIG SYSTEM AND CORRESPONDING WEAK NETWORK

DFIG machine			
Rated Power	7.5 kW	T_d	150 μs 7
R_s	0.44 Ω	R_r	0.64 Ω
$L_{\sigma s}$	3.44 mH	$L_{\sigma r}$	5.16 mH
L_m	79.3 mH	Pole pairs	3
f_s	10 kHz	f_{sw}	5 kHz
LCL filter			
L_g	7 mH	L_f	11 mH
C_f	6.6 μF		
Current controller parameters			
K_{prsc}	4	K_{irsc}	8
K_{pgsc}	4	K_{igsc}	8
PLL controller parameters			
K_{ppll}	1 or 50	K_{ipll}	10 or 500
Three-terminal step-up transformer in DFIG system			
U_G	380 V	U_{SR}	380 V
U_{PCC}	380 V		
$K_1=U_{\mathrm{PCC}}/U_G$	1	$K_2=U_{\mathrm{PCC}}/U_{\mathrm{SR}}$	1
weak network			
L_{NET}	1 mH	R_{NET}	3 mΩ
C_{NET}	200,400 μF		
Two-terminal step-up transformer in weak network			
U_{PCC}	380 V	U_{HV}	380 V
$K_3=U_{\mathrm{HV}}/U_{\mathrm{PCC}}$	1		

$$Z_{G\alpha}(s)=K_2^2\frac{\boldsymbol{U}_{G\alpha}}{-\boldsymbol{I}_{g\alpha}}=K_2^2\frac{1+G_{\mathrm{LCL}}(s)G_{\mathrm{PIGSC}}(s)G_d(s)}{G_{\mathrm{LCL}}(s)} \quad (22a)$$

$$Z_{G\beta}(s)=K_2^2\frac{\boldsymbol{U}_{G\beta}}{-\boldsymbol{I}_{g\beta}}=K_2^2\frac{1+G_{\mathrm{LCL}}(s)\left(1-U_d^{\mathrm{PCC}}T_{\mathrm{PLL}}(s)\right)G_{\mathrm{PIGSC}}(s)G_d(s)\left(1+U_d^{\mathrm{PLL}}T_{\mathrm{PLL}}(s)\right)}{G_{\mathrm{LCL}}(s)}. \quad (22b)$$

TABLE II
PARAMETERS OF 2 MW LARGE-SCALE DFIG SYSTEM AND CORRESPONDING WEAK NETWORK

DFIG machine			
Rated Power	2 MW	T_d	300 μs
R_s	0.0015 Ω	R_r	0.0016 Ω
$L_{\sigma s}$	0.04 mH	$L_{\sigma r}$	0.06 mH
L_m	3 mH	Pole Pairs	3
f_s	5 kHz	$f_{\rm sw}$	2.5 kHz
LCL filter			
L_g	125 μH	L_f	125 μH
C_f	220 μF		
Current controller parameters			
$K_{\rm prsc}$	0.1	$K_{\rm irsc}$	2
$K_{\rm pgsc}$	0.1	$K_{\rm igsc}$	2
PLL controller parameters			
$K_{\rm ppll}$	5 or 50	$K_{\rm ipll}$	50 or 500
Three-terminal step-up transformer in DFIG system			
U_G	480 V	$U_{\rm SR}$	690 V
$U_{\rm PCC}$	1 kV		
$K_1 = U_{\rm PCC}/U_G$	2.08	$K_2 = U_{\rm PCC}/U_{\rm SR}$	1.45
Weak network			
$L_{\rm NET}$	36 mH	$R_{\rm NET}$	2.06 Ω
$C_{\rm NET}$	5 μF, 10 μF		
Two-terminal step-up transformer in weak network			
$U_{\rm PCC}$	1 kV	$U_{\rm HV}$	25 kV
$K_3 = U_{\rm HV}/U_{\rm PCC}$	25		

F. Parallel-Compensated Weak Network Impedance Modeling

The configuration of the parallel-compensated weak network can be seen in Fig. 1, and its impedance modeling can be presented as [15]–[17] follows:

$$Z_{\rm NET} = \frac{1}{K_3^2}\frac{(sL_{\rm NET}+R_{\rm NET})/sC_{\rm NET}}{sL_{\rm NET}+R_{\rm NET}+1/sC_{\rm NET}} \tag{24}$$

where $K_3 = U_{\rm HV}/U_{\rm PCC}$ is the voltage ratio between high voltage $U_{\rm HV}$ in the long-distance transmission cable and PCC voltage $U_{\rm PCC}$.

IV. MFR ANALYSIS

Based on the impedance modeling of the DFIG system concerning the PLL unit in (23) and the parallel-compensated weak network in (24), the MFR can be analyzed.

A. Investigation of MFR

Both a small-scale 7.5 kW and a large-scale 2 MW DFIG system will be discussed, and their parameters are given in Tables I and II.

Fig. 6 shows the Bode diagram of the large-scale DFIG system impedance $Z_{\rm SYS}$ with ①normal PLL control parameters $K_{\rm ppll} = 5$, $K_{\rm ipll} = 50$ and ②fast PLL control parameters $K_{\rm ppll} = 50$, $K_{\rm ipll} = 500$.

By observing Fig. 6, it can be found that, since the α-axis component $Z_{{\rm SYS}\alpha}$ (in yellow) does not involve the PLL unit, its phase response below 800 Hz is smaller than 90°, and a sufficient phase margin can be achieved. Besides, when the PLL with ① normal control parameters $K_{\rm ppll} = 5$, $K_{\rm ipll} = 50$ is involved in the β-axis component $Z_{{\rm SYS}\beta}$ (in red), the phase response is similar to the case of $Z_{{\rm SYS}\alpha}$, indicating no resonance due to a sufficient phase margin.

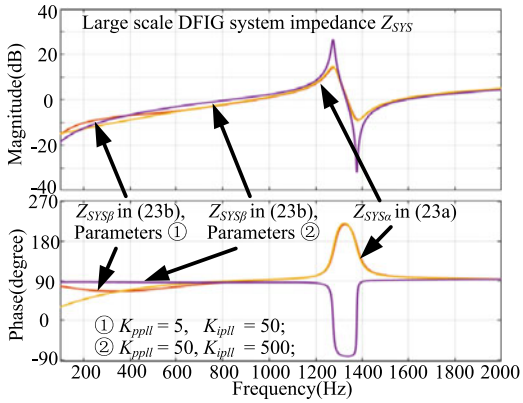

Fig. 6. Bode diagram of 2 MW DFIG system impedance $Z_{\rm SYS}$ with both ①normal PLL control parameters $K_{\rm ppll} = 5$, $K_{\rm ipll} = 50$ and ②fast PLL control parameters $K_{\rm ppll} = 50$, $K_{\rm ipll} = 500$.

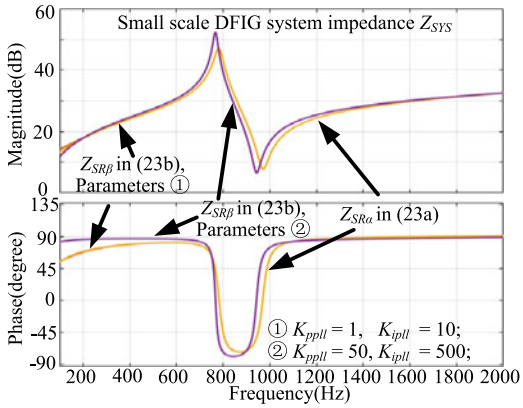

Fig. 7. Bode diagram of 7.5 kW DFIG system impedance $Z_{\rm SYS}$ with both ①normal PLL control parameters $K_{\rm ppll} = 1$, $K_{\rm ipll} = 10$ and ②fast PLL control parameters $K_{\rm ppll} = 50$, $K_{\rm ipll} = 500$.

Nevertheless, when ②fast PLL control parameters $K_{\rm ppll} = 50$, $K_{\rm ipll} = 500$ are assigned to the PLL controller, the phase response of the β-axis component $Z_{{\rm SYS}\beta}$ (in purple) between 200 and 800 Hz is close to 90°, and resonance is very likely to be produced.

On the other hand, Fig. 7 shows the Bode diagram of a small-scale DFIG system impedance $Z_{\rm SYS}$ with both ①normal PLL control parameters $K_{\rm ppll} = 1$, $K_{\rm ipll} = 10$ and ②fast PLL control parameters $K_{\rm ppll} = 50$, $K_{\rm ipll} = 500$.

As it can be seen in Fig. 7, the α-axis component $Z_{{\rm SYS}\alpha}$ (in yellow) and β-axis component $Z_{{\rm SYS}\beta}$ (in red) with ①normal PLL control parameters $K_{\rm ppll} = 1$, $K_{\rm ipll} = 10$ have the same impedance shape, and their phase response below 700 Hz is smaller than 90° and thus no resonance will occur.

However, once the ②fast PLL control parameters $K_{\rm ppll} = 50$, $K_{\rm ipll} = 500$ are employed, its phase response (in purple) is close to 90° and the potential resonance is possible to occur.

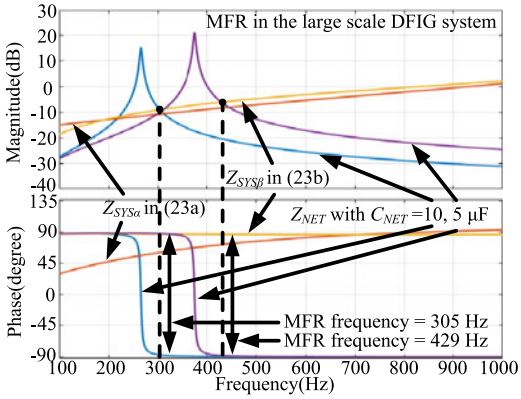

Fig. 8. Bode diagram of the 2 MW DFIG system impedance $Z_{\rm SYS}$ with fast PLL control parameters $K_{\rm ppll} = 50$, $K_{\rm ipll} = 500$, and the parallel-compensated weak network with $C_{\rm NET} = 5, 10\,\mu$F.

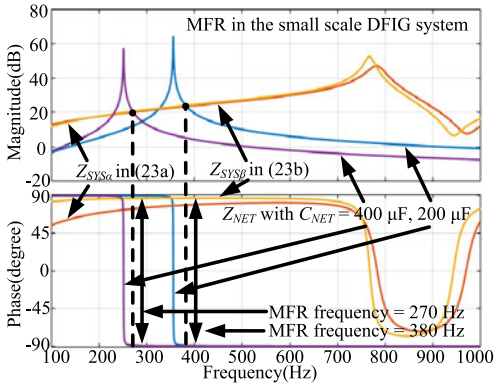

Fig. 9. Bode diagram of the 7.5 kW DFIG system impedance $Z_{\rm SYS}$ with fast PLL control parameters $K_{\rm ppll} = 50$, $K_{\rm ipll} = 500$, and the parallel-compensated weak network with $C_{\rm NET} = 200\,\mu$F, 400 μF.

Therefore, based on the above Bode diagram analysis, it can be concluded that: 1) when the PLL unit is not involved or the PLL unit with normal controller parameters are investigated, no MFR seems to happen due to a sufficient phase margin between 200 and 800 Hz; 2) Once fast controller parameters are adopted in the PLL unit, the phase response of the DFIG system increases close to 90° between 200 and 800 Hz and the phase difference is closer to 180° and the MFR is unfortunately possible to be seen.

Thereafter, the MFR can be analyzed based on the DFIG system impedance with fast PLL controller parameters and the impedance of a parallel-compensated weak network.

Fig. 8 shows the Bode diagram of the 2 MW DFIG system and its corresponding parallel-compensated weak network, their parameters are available in Table II. It can be seen in Fig. 8 that the magnitude intersection points between $Z_{{\rm SYS}\beta}$ and $Z_{\rm NET}$ exist at 305 and 429 Hz, respectively, for the network shunt capacitance $C_{\rm NET} = 10$ and 5 μF, and the phase difference at these two frequencies are close to 180°, then the MFR resonances at 305 and 429 Hz are produced as a consequence.

Note that even $Z_{{\rm SYS}\alpha}$ has magnitude intersection points with the network, but the phase difference is less than 180°, and no resonance will occur due to an acceptable phase margin.

A similar discussion can be achieved for a 7.5 kW DFIG system, as shown in Fig. 9, where a Bode diagram of the small-scale DFIG system and its corresponding parallel-compensated weak network are shown. Their parameters are listed in Table I.

Due to the fast PLL dynamics with large controller parameters, the phase response of the $Z_{{\rm SYS}\beta}$ increases to 90°. Then for the case of the parallel-compensated weak network capacitance $C_{\rm NET} = 400$ and 200 μF, the phase difference of 180° at the magnitude intersection points will produce the MFR at 270 and 380 Hz, respectively.

Therefore, based on the above explanations, it can be concluded that the fast PLL dynamics with large controller parameters cause a phase response of the $Z_{{\rm SYS}\beta}$ increasing to 90°. Thereafter, the phase difference of 180° at the magnitude intersection point between the $Z_{{\rm SYS}\beta}$ and the parallel-compensated weak network $Z_{\rm NET}$ can result in MFR. Moreover, since there is always a decoupling compensation unit in the RSC and GSC control in Figs. 3 and 5, this MFR will also exists in the α-axis component and thus both the large-scale and small-scale DFIG system will suffer from MFR.

B. Stability Boundary of the PLL With the Occurrence of MFR

According to above discussion, the MFR happens when large PI parameters are adopted in the PLL, since the large PI parameters result in the DFIG system phase response increasing to 90° (as shown from red curve to purple curve in Fig. 6 for large-scale DFIG system).

However, the impedance shape of the DFIG system depends on many factors, such as $G_{\rm DFIG}(s), G_{\rm PIRSC}(s), G_d(s)$, and $T_{\rm PLL}(s)$ in the DFIG rotor part impedance in (19), $G_{\rm LCL}(s), G_{\rm PIGSC}(s), G_d(s)$, and $T_{\rm PLL}(s)$ DFIG grid part impedance in (22). Obviously, variations of any factors in (19) and (22) will technically result in an impedance reshaping, thereby partly contribute to the occurrence of the MFR. Therefore, it can be concluded that the PI parameters of the PLL (included in the $T_{\rm PLL}(s)$) are one of the influencing factors, but not the only determining factor of MFR.

Based on above explanation, it is clear that the stability boundary of the PLL regarding the MFR can only be investigated when the parameters of the other influencing factors $G_{\rm DFIG}(s), G_{\rm PIRSC}(s), G_{\rm LCL}(s), G_{\rm PIGSC}(s), G_d(s)$ are specifically assigned. For the purpose of consistency, the following case studies with different PI parameters for the PLL will be conducted using the same parameters used in Figs. 6–9 given in Tables I and II. Only the small-scale DFIG system will be discussed as an example here.

Fig. 10 shows the Bode diagram of the 7.5 kW DFIG system impedance $Z_{\rm SYS}$ with different cases of the PLL control parameters ①$K_{\rm ppll} = 1$, $K_{\rm ipll} = 10$, ②$K_{\rm ppll} = 10$, $K_{\rm ipll} = 100$, ③$K_{\rm ppll} = 20$, $K_{\rm ipll} = 200$, ④$K_{\rm ppll} = 30$, $K_{\rm ipll} = 300$, ⑤ $K_{\rm ppll} = 40$, $K_{\rm ipll} = 400$, ⑥$K_{\rm ppll} = 50$, $K_{\rm ipll} = 500$. It can be seen in Fig. 10 that the when the normal PLL PI parameters as group ①is adopted, the phase response of DFIG system at the potential MFR frequency is 78.2°, thus no MFR will be produced in this case due to the acceptable phase margin.

For the other cases where comparatively larger PI parameters are adopted for the PLL, the phase response of the DFIG system

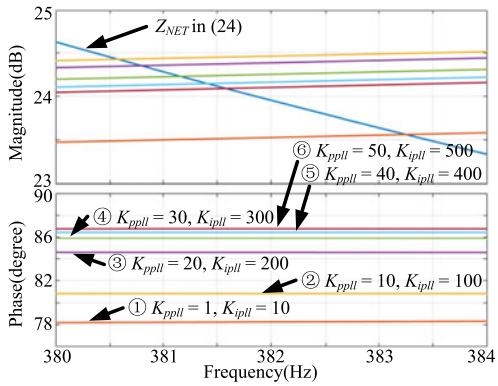

Fig. 10. Bode diagram of the 7.5 kW DFIG system impedance $Z_{\rm SYS}$ with different cases of the PLL control parameters ① $K_{\rm ppll}=1$, $K_{\rm ipll}=10$, ② $K_{\rm ppll}=10$, $K_{\rm ipll}=100$, ③ $K_{\rm ppll}=20$, $K_{\rm ipll}=200$, ④ $K_{\rm ppll}=30$, $K_{\rm ipll}=300$, ⑤ $K_{\rm ppll}=40$, $K_{\rm ipll}=400$, ⑥ $K_{\rm ppll}=50$, $K_{\rm ipll}=500$, and the parallel-compensated weak network with $C_{\rm NET}=200\,\mu$F.

becomes gradually larger and closer to 90° as the PI parameter of PLL becomes larger, that is, 80.8° for the case ②$K_{\rm ppll}=10$, $K_{\rm ipll}=100$, 84.6° for the case ③$K_{\rm ppll}=20$, $K_{\rm ipll}=200$, 85.9° for the case ④$K_{\rm ppll}=30$, $K_{\rm ipll}=300$, 86.5° for the case ⑤$K_{\rm ppll}=40$, $K_{\rm ipll}=400$, and 86.8° for the case ⑥ $K_{\rm ppll}=50$, $K_{\rm ipll}=500$. Thus, based on these results, it can be found that the larger PI parameters for PLL cause the larger phase response of the DFIG system, indicating smaller phase margin, then the MFR is more likely to happen.

Based on above discussion, it can be concluded that

1) The large PI parameter in the PLL ensures a faster PLL dynamic response, but at the same time it is more likely to produce the MFR due to a smaller phase margin.
2) The large PI parameter in the PLL is just one of the many influencing factors, but not the only determining factor. In other words, the larger PI parameters of the PLL contribute just partially, but do not solely determine the occurrence of MFR.
3) According to the discussion in Fig. 10 using several groups of PLL parameters $K_{\rm ppll}$ and $K_{\rm ipll}$, on one hand the larger $K_{\rm ppll}$ and $K_{\rm ipll}$ results in the smaller phase margin, then the MFR is unfortunately more likely to occur as a consequence; while on the other hand, the smaller $K_{\rm ppll}$ and $K_{\rm ipll}$ unfavorably results in slower dynamics response of the PLL, which is not helpful during the grid voltage variation such as low voltage fault.

Hence, it should be noted that the aforementioned acceptable phase margin may vary in different cases, and needs to be appropriately tuned with the consideration of both sufficiently fast dynamic response of the PLL as well as the avoidance of MFR. Normally, the phase margin around 10° is chosen as the case of ①$K_{\rm ppll}=1$, $K_{\rm ipll}=10$ adopted in Fig. 10, the DFIG system performance avoids the MFR and remains sinusoidal, and the appropriate PLL dynamics is ensured as well.

V. Simulation Validation

In order to validate the MFR analysis in both the large-scale and small-scale DFIG system, simulation models are built up. Note that, for the sake of discussion simplicity, the DFIG system impedance modeling in the theoretical section is simplified by removing the mutual inductance branch. However, the simulations are conducted in the MATLAB/Simulink, where the DFIG system is the standard simulation model developed by the MATLAB, and the mutual inductance branch exists. The simplification of removing the mutual inductance branch in the theoretical analysis section does not cause accuracy issues since the mutual inductance is much larger than the stator/rotor leakage inductance. Therefore, the simulation results can be used to validate the theoretical analysis.

A. Simulation Setup and Control Block Diagram

Fig. 11 shows the control block diagram of the DFIG system and its parameters can be found in Tables I and II. The rotor speed is set to 1200 r/min (0.8 p.u.), with the synchronous speed of 1500 r/min (1.0 p.u.).

In the large-scale DFIG system, the dc-link voltage is 1200 V, the switching frequency $f_{\rm sw}$ and the sampling frequency f_s for both RSC and GSC are 2.5 and 5 kHz. In the small-scale DFIG system, the dc-link voltage is 700 V, the switching frequency $f_{\rm sw}$ and the sampling frequency f_s for both RSC and GSC are 5 and 10 kHz.

The SRF-PLL discussed above is employed to provide the information of the PCC voltage fundamental angular speed ω_1 and phase angle θ_1, while an encoder gives the DFIG rotor position θ_r and speed ω_r.

The stator output power control loop first gives out the rotor current reference signals $\boldsymbol{I}^{+*}_{rdq}$. The rotor current $\boldsymbol{I}^{+}_{rdq}$ is sampled and controlled based on the reference value $\boldsymbol{I}^{+*}_{rdq}$ with a PI controller. The output of the rotor current PI closed-loop control and the decoupling compensation are added together, giving the rotor control voltage $\boldsymbol{U}^{+*}_{rdq}$, which is then transformed to the rotor stationary frame and delivered as the input to the space vector pulse width modulation.

As for the GSC control, the dc-link voltage $V_{\rm dc}$ is well controlled by a PI controller, and its output is delivered as the converter side inductance filter current reference $\boldsymbol{I}^{+*}_{fdq}$, which is used to regulate the actual converter side inductance filter current $\boldsymbol{I}^{+}_{fdq}$ by a PI controller. The GSC control voltage $\boldsymbol{U}^{+*}_{gdq}$ can be obtained by the PI current controller output and the decoupling compensation unit.

B. Simulation Results of the Large-Scale DFIG System

Fig. 12 shows the simulation results of the MFR in the 2.0 MW large-scale DFIG system, the parallel-compensated weak network parameters are listed in Table II, $L_{\rm NET}=36$ mH, $R_{\rm NET}=2.06\,\Omega$, $C_{\rm NET}=5\,\mu$F; the PLL controller parameters are normal as $K_{\rm ppll}=5$, $K_{\rm ipll}=50$; or fast as $K_{\rm ppll}=50$, $K_{\rm ipll}=500$.

As it can be seen in Fig. 12(a), before the time = 0.08 s, when the normal controller parameters as $K_{\rm ppll}=5$, $K_{\rm ipll}=50$ are assigned to the PLL controller, the large-scale DFIG system is able to work stable with sinusoidal current, no resonances will exist based on the FFT analysis results shown in Fig. 12(b).

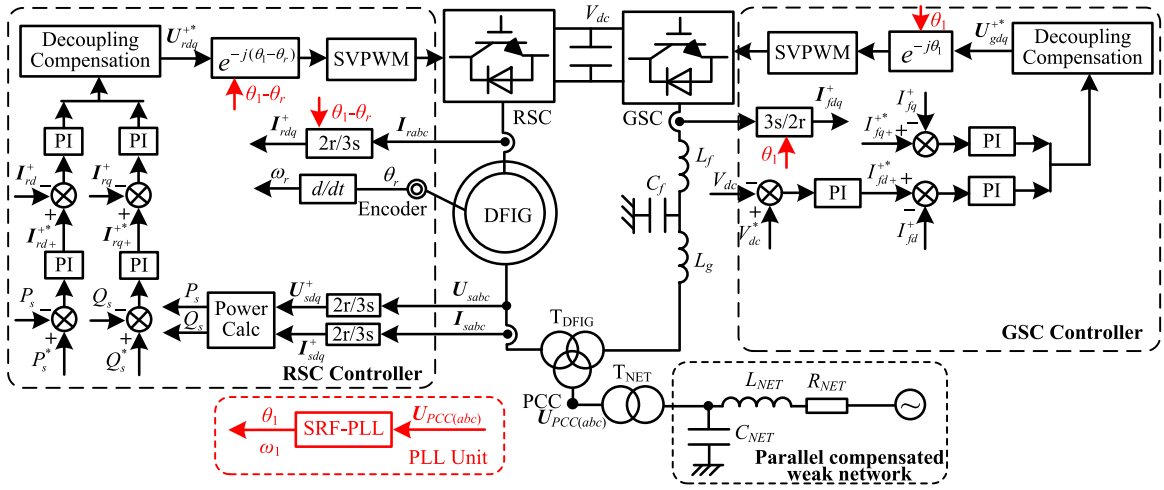

Fig. 11. Overall control block diagram of the DFIG system using SRF-PLL.

On the other hand, once the fast dynamics parameters as $K_{\mathrm{ppll}} = 50$, $K_{\mathrm{ipll}} = 500$ are assigned to the PLL controller, the MFR will occur, and the stator voltage, stator current, rotor current, grid output current, stator output active, and reactive power all contain the resonances components. According to the FFT analysis result of the stator voltage shown in Fig. 12(c), two MFR components occur as 3.81% at –355 Hz and 5.39% at 455 Hz. Similarly, according to the FFT analysis result of the stator current shown in Fig. 12(d), two MFR components occur as 3.18% at –355 Hz and 4.26% at 455 Hz. The resonance components of both stator voltage and stator current are actually in pairs as explained below.

According to the theoretical analysis given in Fig. 8, the magnitude intersection between the DFIG system β-axis $Z_{\mathrm{SYS}\beta}$ and the parallel-compensated weak network Z_{NET} results in the MFR, and this resonance component at the frequency of f_{MFR} will be transformed to the synchronous frame as shown in Fig. 3, thus it behaves as $(f_{\mathrm{MFR}} - 50)$ Hz in the synchronous frame and it will be transformed back to the stationary frame again. As a consequence, the resonance components finally behave in pairs in the stationary frame, i.e., $(f_{\mathrm{MFR}} - 50) + 50 = f_{\mathrm{MFR}}$, and $-(f_{\mathrm{MFR}} - 50) + 50 = -f_{\mathrm{MFR}} + 100$ Hz. This analysis can be verified by the FFT analysis of the stator output active power, as shown in Fig. 12(e). That is, the stator output active power contains only single pulsation component with the frequency of 405 Hz, which is produced by the fundamental component of 50 Hz and the MFR components of +455 and –355 Hz in the stator voltage and stator current.

By comparing the 2 MW DFIG system simulation results of 455 Hz in Fig. 12 and the theoretical results of 429 Hz in Fig. 8, it can be found that the simulation results match well with the theoretical results, then the accuracy of the MFR analysis in the large-scale DFIG system can be verified.

C. Simulation Results of the Small-Scale DFIG System

Fig. 13 shows the simulation results of the MFR in the small-scale DFIG system and the parallel-compensated weak network parameters are listed in Table I, $L_{\mathrm{NET}} = 1$ mH, $R_{\mathrm{NET}} = 3$ mΩ, $C_{\mathrm{NET}} = 200\,\mu$F; the PLL controller parameters are normally as $K_{\mathrm{ppll}} = 1$, $K_{\mathrm{ipll}} = 10$; or fast as $K_{\mathrm{ppll}} = 50$, $K_{\mathrm{ipll}} = 500$.

According to Fig. 13(a), when the normal PLL controller parameters are adopted, i.e., $K_{\mathrm{ppll}} = 1$, $K_{\mathrm{ipll}} = 10$, the small-scale DFIG system is able to work stable without resonances, and the stator voltage FFT analysis shown in Fig. 13(b) helps us to prove this.

In contrast, when the PLL control dynamics become fast using large parameters $K_{\mathrm{ppll}} = 50$, $K_{\mathrm{ipll}} = 500$, the MFR will occur, and the stator voltage, stator current, rotor current, grid output current, stator output active, and reactive power all contain the resonance components, as shown in Fig. 13(a). According to the FFT analysis result of the stator voltage in Fig. 13(c), the stator voltage contains two MFR components 3.37% at –280 Hz and 9.49% at +380 Hz. Similarly, according to the FFT analysis result of the stator current in Fig. 13(d), the stator current also contains two MFR components 16.14% at –280 Hz and 5.87% at +380 Hz. These two components are actually in pairs as discussed above. That is, the stator output power in the small-scale DFIG system contains one single pulsation component of 5.18% at 330 Hz, as shown in Fig. 13(e), which proves that the above resonance components in the stator voltage occur in pairs. Moreover, this simulation result of MFR at 380 Hz matches well with the theoretical analysis in Fig. 9.

Based on the simulation results shown in Figs. 12 and 13, the proposed analysis of MFR caused by the PLL closed-loop control with fast dynamics using large parameters in both the large-scale and small-scale DFIG system can be verified. The MFR is typically seen in the frequency range between 200 and 800 Hz, and occurs in pairs due to the reference frame transformation between the stationary frame and the synchronous frame.

It should be pointed out that in the theoretical analysis Section III. B, the DFIG machine is modeled using its equivalent circuit shown in Fig. 4, and the mutual inductance branch is neglected for the sake of analysis simplification. However,

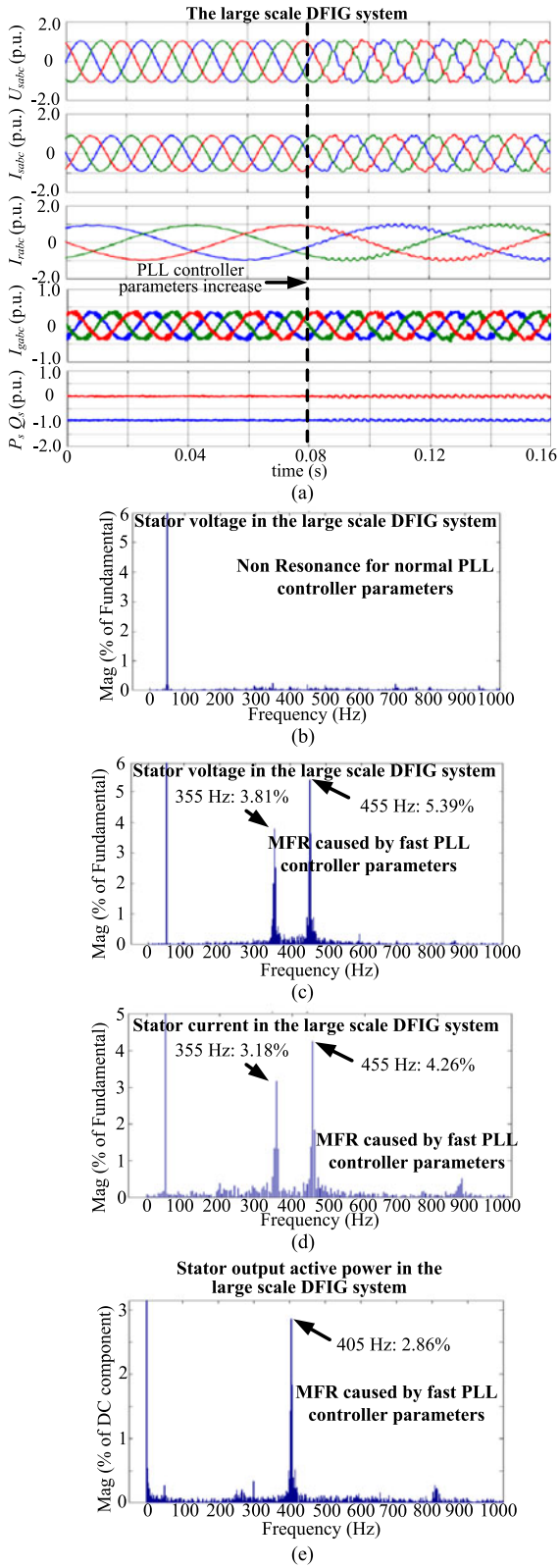

Fig. 12. Simulation results of the MFR in the 2 MW DFIG system, the parallel-compensated weak network parameters are listed in Table II, $L_{\mathrm{NET}} = 36$ mH, $R_{\mathrm{NET}} = 2.06\,\Omega$, $C_{\mathrm{NET}} = 5\,\mu$F; the PLL controller parameters are normally as $K_{\mathrm{ppll}} = 5$, $K_{\mathrm{ipll}} = 50$; or fast as $K_{\mathrm{ppll}} = 50$, $K_{\mathrm{ipll}} = 500$. (a) DFIG system performance; (b) stator voltage FFT analysis without resonance; (c) stator voltage FFT analysis with MFR; (d) stator current FFT analysis with MFR; and (e) stator output active power FFT analysis with MFR.

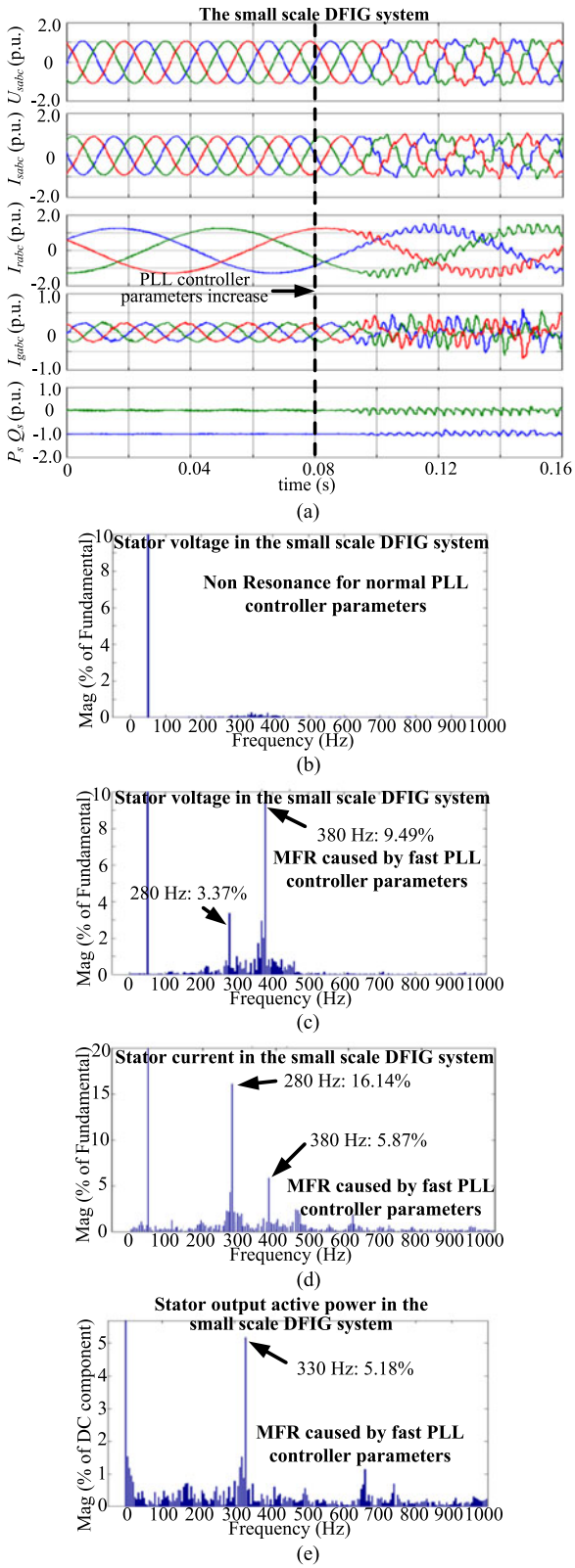

Fig. 13. Simulation results of the MFR in the 7.5 kW DFIG system, the parallel-compensated weak network parameters are listed in Table I, $L_{\mathrm{NET}} = 1$ mH, $R_{\mathrm{NET}} = 3$ mΩ, $C_{\mathrm{NET}} = 200\,\mu$F; the PLL controller parameters are normally as $K_{\mathrm{ppll}} = 1$, $K_{\mathrm{ipll}} = 10$; or fast as $K_{\mathrm{ppll}} = 50$, $K_{\mathrm{ipll}} = 500$. (a) DFIG system performance; (b) stator voltage FFT analysis without resonance; (c) stator voltage FFT analysis with MFR; (d) stator current FFT analysis with MFR; and (e) stator output active power FFT analysis with MFR.

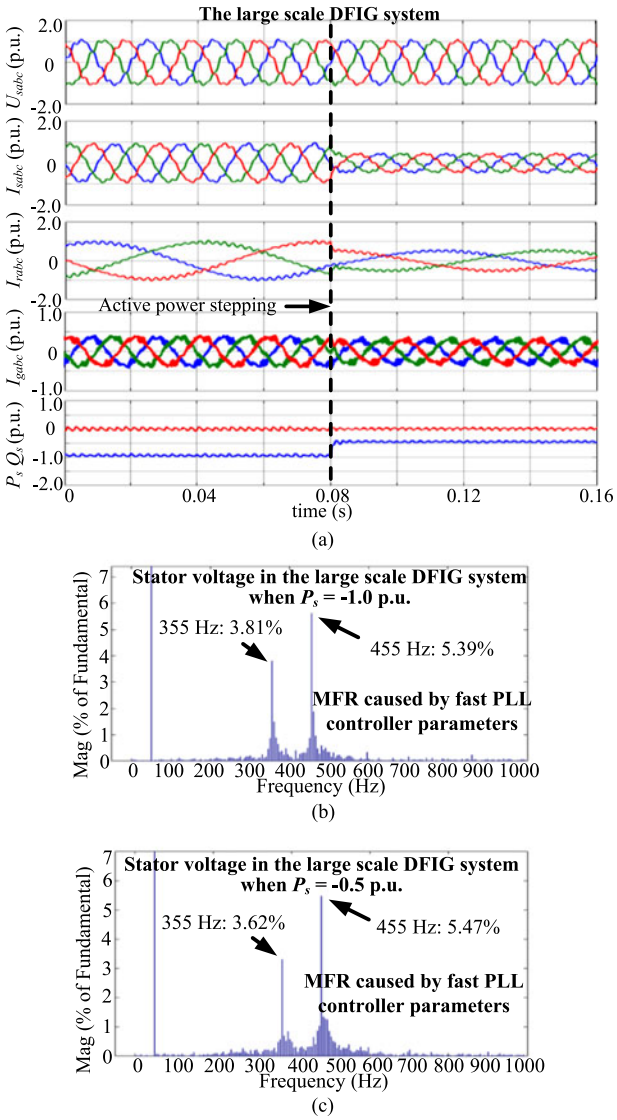

Fig. 14. Simulation results of active power step from 1.0 to 0.5 p.u. in the large-scale 2 MW DFIG system, the parallel-compensated weak network parameters are listed in Table II, $L_{\rm NET} = 36$ mH, $R_{\rm NET} = 2.06\,\Omega$, $C_{\rm NET} = 5\,\mu$F; the PLL controller parameters are fast as $K_{\rm ppll} = 50$, $K_{\rm ipll} = 500$. (a) DFIG system performance; (b) stator voltage FFT analysis before active power stepping, $P_s = -1.0$ p.u.; (c) stator voltage FFT analysis after the active power step, $P_s = -0.5$ p.u..

in the simulation based on the MATLAB/Simulink, the DFIG machine is simulated using a complete DFIG machine model provided by the Simulink, which is more accurate but also more complicated. Therefore, the small difference in the MFR frequencies between the theoretical analysis and the simulation is due to the simplified DFIG machine model used in the analysis and the detailed DFIG machine model used in Simulink.

D. Simulation Results of Active Power Step in the Large-Scale DFIG System

Fig. 14 shows the simulation results when an active power step is done from 1.0 to 0.5 p.u. in the large-scale 2 MW DFIG system, using the parallel-compensated weak network parameters as listed in Table II, $L_{\rm NET} = 36$ mH, $R_{\rm NET} = 2.06\,\Omega$, $C_{\rm NET} = 5\,\mu$F; the PLL controller parameters are fast as $K_{\rm ppll} = 50$, $K_{\rm ipll} = 500$. Fig. 14(a) shows the DFIG system performance, and Fig. 14(b) shows the stator voltage FFT analysis before the active power step, $P_s = -1.0$ p.u.; Fig. 14(c) shows the stator voltage FFT analysis after the active power step, $P_s = -0.5$ p.u.;

It can be seen in Fig. 14(a) that both before and after the active power step, the MFR exists in the DFIG system and it proves that the occurrence of MFR is independent of the DFIG output active power variation. Moreover, even in the existence of MFR, the stator output active power is able to follow the reference precisely, which means the MFR will not result in the failure of the DFIG system operation, but jeopardizing the output wind power quality by injecting current resonance components into the power grid.

Besides, by comparing the stator voltage harmonic analysis before and after the active power step in Fig. 14(b) and (c), it can be seen that the resonance components remain almost the same at different active power output. Similar conclusions regarding the stator current and output power can be deduced, but they are not shown here for the sake of simplicity.

VI. Conclusion

This paper has investigated the MFR of the DFIG system considering the PLL control with fast PLL control dynamics using large controller parameters. Several conclusions can be obtained:

1) When the normal PLL controller parameters are adopted, the DFIG system is able to work stable without resonance due to an acceptable phase margin;
2) However, the PLL with fast dynamics using large controller parameters will increase the phase response of the DFIG system closer to 90°, and consequently result in MFR. The frequency range of the MFR is typically between 200 and 800 Hz due to the phase response character of the DFIG system. The MFR resonance components occur often in pairs due to the reference frame transformation between the stationary frame and the synchronous frame.
3) In a normal practical situation, the MFR can be avoided by appropriately adjusting the PLL controller parameters, while ensuring a sufficiently fast PLL dynamics at the same time. This indicates that the active damping strategy for the MFR is unnecessary.

References

[1] F. Blaabjerg and K. Ma, "Future on power electronics for wind turbine systems," *IEEE J. Emerg. Sel. Top. Power Electron.*, vol. 1, no. 3, pp. 139–152, Sep. 2013.
[2] K. Ma, L. Tutelea, I. Boldea, D. M. Ionel, and F. Blaabjerg, "Power electronic drives, controls, and electric generators for large wind turbines—An overview," *Elect. Power Compon. Syst.*, vol. 43, no. 12, pp. 1406–1421, 2015.
[3] V. Yaramasu, B. Wu, P. C. Sen, S. Kouro, and M. Narimani, "High-power wind energy conversion systems: State-of-the-art and emerging technologies," *Proc. IEEE*, vol. 103, no. 5, pp. 740–788, May 2015.
[4] H. Nian, P. Cheng, and Z. Q. Zhu, "Independent operation of DFIG-based WECS using resonant feedback compensators under unbalanced grid voltage conditions," *IEEE Trans. Power Electron.*, vol. 30, no. 7, pp. 3650–3661, Jul. 2015.

[5] H. Nian, P. Cheng, and Z. Q. Zhu, "Coordinated direct power control of DFIG system without phase-locked loop under unbalanced grid voltage conditions," *IEEE Trans. Power Electron.*, vol. 31, no. 4, pp. 2905–2918, Apr. 2016.
[6] J. Hu, B. Wang, W. Wang, H. Tang, Y. Chi, and Q. Hu., "Small signal dynamics of DFIG-based wind turbines during riding through symmetrical faults in weak AC grid," *IEEE Trans. Energy Convers.*, to be published.
[7] J. Hu, L. Sun, X. Yuan, S. Wang, and Y. Chi, "Modeling of type 3 wind turbine with df/dt inertia control for system frequency response study," *IEEE Trans. Power Syst.*, to be published.
[8] I. Vieto and J. Sun, "Damping of subsynchronous resonance involving type-III wind turbines," in *Proc. Control Model. Power Electron.*, 2015, pp. 1–8.
[9] I. Vieto and J. Sun, "Small-signal impedance modeling of type-III wind turbine," in *Proc. Power Energy Soc. Gen. Meeting*, 2015, pp. 1–5.
[10] I. Vieto and J. Sun, "Real-time simulation of subsynchronous resonance in type-III wind turbines," in *Proc. Control Model. Power Electron.*, 2014, pp. 1–8.
[11] Z. Miao, "Impedance-model-based SSR analysis for type 3 wind generator and series-compensated network," *IEEE Trans. Energy Convers.*, vol. 27, no. 4, pp. 984–991, Dec. 2012.
[12] L. Piyasinghe, Z. Miao, J. Khazaei, and L. Fan, "Impedance model-based SSR analysis for TCSC compensated type-3 wind energy delivery systems," *IEEE Trans. Sustain. Energy*, vol. 6, no. 1, pp. 179–187, Jan. 2015.
[13] L. Fan and Z. Miao, "Nyquist-stability-criterion-based SSR explanation for type-3 wind generators," *IEEE Trans. Energy Convers.*, vol. 27, no. 3, pp. 807–809, Sep. 2012.
[14] L. Fan and Z. Miao, "Mitigating SSR using DFIG-based wind generation," *IEEE Trans. Sustain. Energy*, vol. 3, no. 3, pp. 349–358, Jul. 2012.
[15] Y. Song, X. Wang, and F. Blaabjerg, "High frequency resonance damping of DFIG based wind power system under weak network," *IEEE Trans. Power Electron.*, vol. 32, no. 3, pp. 1927–1940, Mar. 2017.
[16] Y. Song, X. Wang, and F. Blaabjerg, "Impedance-based high frequency resonance analysis of DFIG system in weak grids," *IEEE Trans. Power Electron.*, vol. 32, no. 5, pp. 3536–3548, May 2017.
[17] Y. Song and F. Blaabjerg, "Wide frequency band active damping strategy for DFIG system high frequency resonance," *IEEE Trans. Energy., Convers.*, vol. 31, no. 4, pp. 1665–1675, Dec. 2016.
[18] X. Wang, F. Blaabjerg, and P. C. Loh, "Grid-current-feedback active damping for LCL resonance in grid-connected voltage source converters," *IEEE Trans. Power Electron.*, vol. 31, no. 1, pp. 213–223, Jan. 2016.
[19] X. Wang, F. Blaabjerg, and P. C. Loh, "Virtual RC damping of LCL-filtered voltage source converters with extended selective harmonic compensation," *IEEE Trans. Power Electron.*, vol. 30, no. 9, pp. 4726–4737, Sep. 2015.
[20] X. Wang, F. Blaabjerg, and W. Wu, "Modeling and analysis of harmonic stability in an AC power-electronics-based power system," *IEEE Trans. Power Electron.*, vol. 29, no. 12, pp. 6421–6432, Dec. 2014.
[21] X. Wang, Y. Li, F. Blaabjerg, and P. C. Loh, "Virtual-impedance-based control for voltage-source and current-source converters," *IEEE Trans. Power Electron.*, vol. 30, no. 12, pp. 7019–7037, Dec. 2015.
[22] C. Bao, X. Ruan, X. Wang, W. Li, D. Pan, and K. Weng, "Step-by-step controller design for LCL-type grid-connected inverter with capacitor–current-feedback active-damping," *IEEE Trans. Power Electron.*, vol. 29, no. 3, pp. 1239–1253, Mar. 2014.
[23] D. Pan, X. Ruan, C. Bao, W. Li, and X. Wang, "Optimized controller design for LCL-type grid-connected inverter to achieve high robustness against grid-impedance variation," *IEEE Trans. Ind. Electron.*, vol. 62, no. 3, pp. 1537–1547, Mar. 2015.
[24] D. Pan, X. Ruan, C. Bao, W. Li, and X. Wang, "Capacitor-current-feedback active damping with reduced computation delay for improving robustness of LCL-type grid-connected inverter," *IEEE Trans. Power Electron.*, vol. 29, no. 7, pp. 3414–3427, Jul. 2014.
[25] D. Yang, X. Ruan, and H. Wu, "A real-time computation method with dual sampling mode to improve the current control performance of the LCL-type grid-connected inverter," *IEEE Trans. Ind. Electron.*, vol. 62, no. 7, pp. 4563–4572, Jul. 2015.
[26] B. Wen, D. Boroyevich, R. Burgos, P. Mattavelli, and Z. Shen, "Analysis of D-Q small-signal impedance of grid-tied inverters," *IEEE Trans. Power Electron.*, vol. 31, no. 1, pp. 675–687, Jan. 2016.
[27] B. Wen, D. Boroyevich, R. Burgos, P. Mattavelli, and Z. Shen, "Small-signal stability analysis of three-phase AC systems in the presence of constant power loads based on measured d-q frame impedances," *IEEE Trans. Power Electron.*, vol. 30, no. 10, pp. 5952–5963, Oct. 2015.

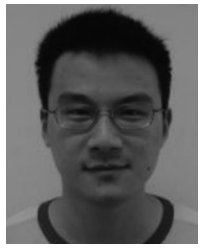

Yipeng Song (M'16) was born in Hangzhou, China. He received the B.Sc. degree from the College of Electrical Engineering, Zhejiang University, Hangzhou, in 2010, and Ph.D. degree in improved control strategy of doubly fed induction generator under unbalanced and distorted grid voltage from the College of Electrical Engineering, Zhejiang University, Hangzhou, in 2015.

He is currently working as a Postdoctoral Researcher in the Department of Energy Technology, Aalborg University, Aalborg, Denmark. His current research interests include motor control with power electronics devices in renewable-energy conversion, particularly the control and operation of doubly fed induction generators for wind power generation.

Frede Blaabjerg (S'86–M'88–SM'97–F'03) received the Ph.D. degree in control of power electronics converters from Aalborg University, Aalborg, Denmark, in 1992.

From 1987 to 1988, he was with ABB-Scandia, Randers, Denmark. He became an Assistant Professor in 1992, an Associate Professor in 1996, and a Full Professor of power electronics and drives in 1998. His current research interests include power electronics and its applications, such as in wind turbines, PV systems, reliability, harmonics, and adjustable speed drives.

Dr. Blaabjerg was an Editor-in-Chief of the IEEE TRANSACTIONS ON POWER ELECTRONICS from 2006 to 2012. He received the 17 IEEE Prize Paper Awards, the IEEE PELS Distinguished Service Award in 2009, the EPE-PEMC Council Award in 2010, the IEEE William E. Newell Power Electronics Award 2014, and the Villum Kann Rasmussen Research Award 2014. He is nominated in 2014 and 2015 by Thomson Reuters to be between the most 250 cited researchers in Engineering in the world.